



저작자표시-비영리-변경금지 2.0 대한민국

이용자는 아래의 조건을 따르는 경우에 한하여 자유롭게

- 이 저작물을 복제, 배포, 전송, 전시, 공연 및 방송할 수 있습니다.

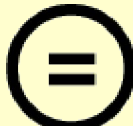
다음과 같은 조건을 따라야 합니다:



저작자표시. 귀하는 원 저작자를 표시하여야 합니다.



비영리. 귀하는 이 저작물을 영리 목적으로 이용할 수 없습니다.



변경금지. 귀하는 이 저작물을 개작, 변형 또는 가공할 수 없습니다.

- 귀하는, 이 저작물의 재이용이나 배포의 경우, 이 저작물에 적용된 이용허락조건을 명확하게 나타내어야 합니다.
- 저작권자로부터 별도의 허가를 받으면 이러한 조건들은 적용되지 않습니다.

저작권법에 따른 이용자의 권리와 책임은 위의 내용에 의하여 영향을 받지 않습니다.

이것은 [이용허락규약\(Legal Code\)](#)을 이해하기 쉽게 요약한 것입니다.

[Disclaimer](#)



A Study on Twinkling Artifact for Detecting Breast Microcalcifications



December 2024

The Graduate School of Sogang University
Department of Electronic Engineering
Seongjun Park

A Study on Twinkling Artifact for Detecting Breast Microcalcifications

지도교수 유 양 모

이 논문을 공학석사 학위논문으로 제출함

2024년 12월

서강대학교 대학원

전자공학과

박성준



논문 인준서

박성준의 공학석사 학위논문을 인준함

2024년 12월

주심 최 용 (인)

부심 유 양 모 (인)

부심 배 수 아 (인)



넘치는 사랑의 덕으로 27 살의 박성준이 되어 부족하지만 자랑스러운 학위논문을 완성합니다.
저를 응원해 주시고, 지혜를 선물해주신 가족, 친구, 선배, 은사님들을 향한 끝없는 감사함을,
영원히 기억하겠습니다.

2024.12.

박성준



Contents

Abstract.....	5
I. Introduction.....	6
A. Breast cancer and microcalcifications.....	6
B. Twinkling artifacts for microcalcification detection.....	7
C. Research motivation.....	8
II. Ultrasound Doppler system.....	9
A. CW Doppler system.....	10
B. PW Doppler system	13
C. Color Doppler system	16
III. Autocorrelation based Doppler classifier	17
A. Preliminary study	18
B. Autocorrelation based Feature extraction	19
C. Dataset organization and Classifier training	22
IV. Multi band Doppler imaging	26
A. Hypothesis.....	26
B. MBDI signal block.....	27
C. Filter bank	28
D. Signal modeling and weight optimization.....	29



E. Visualization	31
V. Experimental result	32
A. Experimental setup.....	32
B. Experimental results.....	35
VI. Discussion and Conclusions	43
A. Discussion.....	43
B. Conclusions.....	46
Reference	48



List of Figures

Figure 1. Illustration of Data receive sequence in color Doppler	17
Figure 2. Signal characteristics of TA, Flow and noise.....	18
Figure 3. Phantom setup for machine learning dataset	23
Figure 4. Scatter plot of extracted features from the dataset for each parameter.....	24
Figure 5. Overall signal processing block diagram.....	27
Figure 6. Illustration of filter bank structure and output data	28
Figure 7. Concept of signal vector modeling method	30
Figure 8. Visualization of the Proposed Method.....	31
Figure 9. Fabrication of the Phantom.....	33
Figure 10. Experimental setup using the fabricated phantom	34
Figure 11. Qualitative results of the MBDI method.....	36
Figure 12. Result image of proposed Doppler classifier	38
Figure 13. Experimental results of <i>in-vivo</i> breast	39
Figure 14. Experimental results of <i>in-vivo</i> breast	40
Figure 15. Experimental results of <i>in-vivo</i> breast	41
Figure 16. Experimental results of <i>in-vivo</i> breast	42
Figure 17. Comparison of the proposed method and conventional average frequency estimation methods.	45



List of Tables

Table 1. Experimental parameters for dataset organization	24
Tabel 2. Validation accuracy of the dataset for each model	25
Table 3. Transmit-Receive parameters for experiment	34
Tabel 4. quantitative result of MBDI method	37



ABSTRACT

Breast cancer is characterized by high incidence and mortality rates, as well as poor prognosis in advanced stages. Effective screening techniques are therefore critical for its management, with X-ray-based mammography currently serving as the standard method. However, mammography has limitations, including radiation exposure and patient discomfort, driving interest in ultrasound-based approaches for early detection. Recent research has focused on utilizing the Twinkling Artifact (TA) to detect microcalcifications (MCs) in breast tissue, aiming to enhance sensitivity in early breast cancer diagnosis.

Existing studies, however, have limited consideration to in-vivo environments where diverse noise sources are present. Moreover, the detection of TA has traditionally relied on examiners, posing another limitation. To address these challenges, this study proposes a machine learning-based method for the automatic detection and classification of TA. Additionally, a filter bank technique is utilized to enhance TA signals adaptively. The proposed method achieved classification accuracy exceeding 97% and demonstrated signal amplification performance above 110dB. Notably, applicability of the classifier was validated through in-vivo experiments, highlighting its potential for practical implementation. These results suggest that the proposed techniques can serve as robust and automated solutions for TA detection in clinical settings.



I. Introduction

A. Breast cancer and microcalcifications

Breast cancer is a high-risk disease characterized by significant incidence and mortality rates [1]. According to Global Cancer Statistics (GLOBOCAN), approximately 2.29 million new cases of breast cancer were diagnosed worldwide in 2022, resulting in 660,000 deaths [2]. This marks breast cancer as the most prevalent and deadly cancer among women globally. The incidence of breast cancer is expected to continue rising in the coming years [3]. Moreover, breast cancer becomes increasingly life-threatening as it progresses beyond its early stages. The 5-year survival rate exceeds 90% when breast cancer is detected at stage I or II but drops to 75% at stage III and plummets to 29% at stage IV [4-5]. Thus, early detection and effective screening techniques are essential for mitigating the risks associated with breast cancer.

Currently, X-ray mammography is the standard screening technique for breast cancer detection [6-7]. Mammography visualizes key breast cancer indicators, such as mass formation, structural distortion, and the presence of microcalcifications (MCs), by capturing X-ray images [8]. Among these indicators, MCs—accumulations of calcium deposits within the tissue—are particularly associated with early-stage breast cancer [9-11]. Therefore, the detection of MCs is crucial for early diagnosis, positioning mammography as the primary standard for breast cancer screening. However, mammography involves radiation exposure, which inherently increases the risk of



radiation-induced cancer [12]. Furthermore, in women with dense breasts—a condition more prevalent among Asian women—the sensitivity of mammography decreases significantly. Studies comparing dense and fatty breasts in women over 50 years old reported up to a 14.7 percentage point reduction in mammography sensitivity [13]. Additionally, mammography causes considerable discomfort during the procedure, potentially reducing patient compliance and participation in regular screenings [14].

Given these limitations, alternative imaging techniques have been explored to substitute mammography. Potential methods for visualizing MCs include magnetic resonance imaging (MRI) and ultrasound imaging [6]. MRI offers advantages such as the absence of radiation exposure and high contrast resolution. However, its high cost and long examination times limit its applicability as a routine screening method. In contrast, ultrasound imaging provides several advantages, including no radiation exposure, low examination costs, high accessibility, and real-time imaging capabilities [15]. Despite these benefits, ultrasound imaging suffers from low contrast resolution, which restricts its current applications to limited uses, such as the observation of masses [16]. As a result, the standalone use of ultrasound for detecting MCs in early breast cancer diagnosis remains challenging.

B. Twinkling artifacts for microcalcification detection

Recently, studies have focused on improving the sensitivity of detecting microcalcifications (MCs) by utilizing the Twinkling Artifact (TA). TA refers to the



appearance of random Doppler signals when imaging rough surfaces in color Doppler mode [17-18]. It has been discussed that TA can be used for detecting calcified materials since it occurs on the surfaces of calcified crystals within the body [19].

TA has also been observed from MCs, which are calcified deposits within the breast tissue. Consequently, the potential for effective MCs detection using TA has been reported [20]. Further research has explored optimal transmission conditions to enhance the detection of MCs [21]. The other study has reported that transmitting ultrasound with uniformly high mechanical index (MI) values across a broad region of interest (ROI) enables the detection of MCs in specimens from mastectomy patients. [22]. However, these studies are limited to laboratory settings and lack consideration of in-vivo environments.

In-vivo, diverse Doppler signals such as those from blood flow act as significant noise sources, complicating TA detection. Additionally, there has been insufficient research on techniques to amplify received TA signals and effectively visualize TA amidst diverse Doppler signals. Consequently, the sensitivity of TA detection remains limited, relying on the examiner's experience.

C. Research motivation

This study aims to propose an effective method for detecting MCs using TA. It addresses the limitations of prior research, which limited to considering the coexistence of blood flow and TA signals. In scenarios where these signals coexist, distinguishing



between them often depends on the examiner's expertise. To develop automated diagnostic systems or establish quantifiable diagnostic criteria, distinguishing these signals is essential. Therefore, this study investigates the characteristics of TA and blood flow signals, proposing a machine learning-based algorithm to automate their differentiation.

Moreover, this study also addresses the lack of techniques to amplify TA signals. Without amplification, TA signals—it can be weaker than system noise in color Doppler mode—may remain undetectable. To address this, the study proposes a method to adaptively enhance TA signals, thereby improving the sensitivity of TA-based MCs detection.

The structure of this paper is as follows: Section 2 provides an overview of conventional ultrasound Doppler systems. Section 3 introduces a machine learning-based classification algorithm to distinguish TA from blood flow signals. Section 4 presents a technique for adaptively amplifying TA signals. Section 5 validates the proposed methods through experimental results, followed by a discussion in Section 6.

II. Ultrasound Doppler system

An ultrasound imaging system transmits high-frequency sound waves (above the audible range) into the body and receives reflected waves to visualize anatomical structures [15,23]. Ultrasound, as a wave, interacts with red blood cells (RBCs) in the bloodstream, which reflect the sound waves. When these reflectors move, a frequency



shift occurs in the reflected waves depending on their velocity. This phenomenon is known as the Doppler effect. Doppler ultrasound utilizes this effect to measure blood flow velocity by observing frequency changes after transmitting sound waves into regions containing blood flow [24]. This section provides an overview of Doppler ultrasound systems, clarifying the terminology and concepts used in this paper.

A. CW Doppler system

The Doppler effect refers to the phenomenon in which the frequency of a wave changes when the wave source is in motion or when the wave is reflected off a moving object. This effect occurs in medical ultrasound as well; when ultrasound waves are reflected by moving red blood cells (RBCs), their frequency shifts. The Doppler shift frequency, f_d , can be determined using Equation (1) [25].

$$f_d = \frac{2vf_0}{c} \cos\theta \quad (1)$$

Here, f_d denotes the Doppler shift frequency, v is the velocity of the RBCs, c represents the speed of the ultrasound, f_0 is the transmitted wave frequency, and θ is the angle between the blood flow direction and the ultrasound beam. For simplicity, subsequent discussions assume θ is 0, and the equations are presented accordingly.

To obtain the reflected wave with a Doppler shift, an ultrasound transducer must transmit an ultrasound signal. In systems where the transmitted wave is a continuous



sinusoidal signal, this configuration is referred to as a continuous wave (CW) Doppler system. [26]. The transmitted wave can be expressed as a function in Equation (2):

$$f(t) = \cos 2\pi f_0 t \quad (2)$$

When the continuous wave described by Equation (2) is reflected by RBCs and received, the Doppler shift occurs as shown in Equation (3):

$$r(t) = a(t) \cos[2\pi(f_0 + f_d)t + \phi] \quad (3)$$

Here, $a(t)$ represents the envelope function arising from the reflection process, and ϕ is the phase angle induced by the transmission-reception path. Since ϕ is a very small constant, it is neglected. To calculate f_d from the received wave, a downshift process is performed, ensuring the sign of f_d is preserved. This preservation is critical for detecting both the velocity and direction of blood flow. Therefore, the CW Doppler system employs quadrature demodulation (QDM).

To extract the in-phase component of the received wave $r(t)$, it is multiplied by a cosine function, resulting in Equation (4):

$$a(t) \cos[2\pi(f_0 + f_d)t] \cos 2\pi f_0 t \quad (4)$$

Using trigonometric properties, Equation (4) simplifies to:



$$\frac{a(t)}{2} \{ \cos[2\pi f_d t] + \cos[2\pi(2f_0 + f_d)t] \} \quad (5)$$

Applying a low-pass filter to remove high-frequency components yields:

$$I(t) = \frac{1}{2} a(t) \cos 2\pi f_d t \quad (6)$$

The quadrature component can be obtained by multiplying the signal with a sine function, resulting in:

$$Q(t) = \frac{1}{2} a(t) \sin 2\pi f_d t \quad (7)$$

These two components, the in-phase and quadrature signals, can be expressed in the form of a complex function $z(t)$ as:

$$I(t) + jQ(t) = z(t) = \frac{a(t)}{2} e^{j2\pi f_d t} \quad (8)$$

By applying the Fast Fourier Transform (FFT) to $z(t)$, the value of f_d can be determined. However, there are additional signals not considered in the above equations. These are signals reflected from stationary or very slow-moving objects, referred to as clutter signals. In Doppler ultrasound, clutter signals are characterized by low Doppler frequencies and high amplitudes. Including clutter components in Equation (8) leads to Equation (9):



$$z(t) = \frac{a_c(t)}{2} e^{j2\pi f_c t} + \frac{a(t)}{2} e^{j2\pi f_d t} \quad (9)$$

Here, f_c represents the Doppler shift frequency of the clutter signal, and $a_c(t)$ is the amplitude of the clutter signal, which is significantly larger than $a(t)$. Consequently, when $z(t)$ is transformed using the FFT, the large clutter signal may dominate the dynamic range, obscuring details of the flow signal with smaller amplitudes. Suppressing clutter signals is therefore desirable and is achieved through a process known as clutter filtering. Clutter filtering can be implemented by applying an appropriate high-pass filter with a defined cutoff frequency to the IQ or complex signal.

B. PW Doppler system

While CW Doppler can measure both the velocity and direction of blood flow, it has the limitation of not providing depth information about the target. Ultrasound imaging systems typically acquire depth information using the time of flight (TOF), which is the time taken for an ultrasound pulse to travel to and from the target. However, since CW Doppler uses continuous waveforms, the received signal is continuous as well, making it impossible to correlate the received signal with a specific transmission event. As a result, CW Doppler cannot determine the depth of the target. To simultaneously obtain both the velocity and positional information of blood flow, a Pulsed Wave (PW) Doppler system can be used.



PW Doppler transmits a limited number of cycles in each pulse. Due to this limitation, there are insufficient samples for determining the Doppler frequency using FFT as in CW Doppler. To address this, PW Doppler transmits multiple pulse waves at regular intervals. The time interval between pulses is referred to as the Pulse Repetition Interval (PRI), and the frequency of pulse transmissions is called the Pulse Repetition Frequency (PRF). Now, let the k -th pulse signal be represented by Equation (10), and the received wave corresponding to it as Equation (11):

$$f(t) = \text{rect}(t) \cdot \cos 2\pi f_0 t \quad (10)$$

$$r_k(t) = a(t) \cos[2\pi(f_0 + f_d)t + \phi(k)] \quad (11)$$

where $\phi(k)$ represents the phase shift of the received wave caused by differences in the time of flight (TOF) due to the motion of red blood cells (RBCs). The variable k refers to the index of the transmitted pulse. As mentioned earlier, due to the limited number of samples, PW Doppler cannot directly determine f_d using FFT. Instead, it calculates blood flow velocity by detecting minute changes in $\phi(k)$. To analyze $\phi(k)$, consider Equation (12):

$$\phi(k+1) - \phi(k) = \Delta\phi = 2(v \cdot PRI) \frac{2\pi}{\lambda} \quad (12)$$

This equation converts the displacement of RBCs into a phase angle. The factor of 2 accounts for the doubled TOF difference due to the round-trip travel of the ultrasound,



$v \cdot PRI$ represents the RBC displacement between pulses, and $\frac{2\pi}{\lambda}$ is the coefficient for converting distance into a phase angle. Substituting Equation (1) into Equation (12) yields:

$$\Delta\phi = 2\pi \cdot f_d \cdot \frac{1}{PRF} \quad (13)$$

Equation (13) demonstrates that the Doppler frequency can be indirectly determined using $\Delta\phi$.

By applying quadrature demodulation to the received pulse $r_k(t)$, as described in Equation (10), the complex signal can be expressed as:

$$I_k(t) + jQ_k(t) = z_k(t) = \frac{a_k(t)}{2} e^{j(2\pi f_d t + \frac{2\pi f_d k}{PRF})} \quad (14)$$

Here, $I_k(t)$, $Q_k(t)$ and $z_k(t)$ represent the in-phase, quadrature, and complex signals of the k -th pulse, respectively. Although the number of samples in the t -direction is limited, performing FFT along the pulse index (k) direction allows the determination of Doppler frequency. This principle forms the basis of PW Doppler, which calculates blood flow velocity.

PW Doppler can be implemented in applications such as spectral Doppler and Color Doppler Imaging (CDI). This study focuses on CDI, and its methodology is introduced below.



C. Color Doppler Imaging

Color Doppler Imaging (CDI) differs from spectral Doppler in that it applies PW Doppler over a broad ROI. CDI visualizes the average Doppler frequencies across a wide area using various colors, providing hemodynamic information. Since CDI involves imaging a broad area, the number of transmitted pulses must be carefully determined. A series of transmitted pulses in CDI is referred to as an ensemble, and the number of pulses sent to a single point is called the ensemble length. While increasing the ensemble length improves signal quality, it also reduces the overall frame rate due to the need to transmit more pulses across the imaging area. Consequently, the ensemble length in CDI is typically limited. A schematic representation of the data transmission and reception sequence in CDI is shown in Fig. 1.

As depicted in Fig. 1, CDI transmits and receives pulses corresponding to the ensemble length along a single scan line. This process is repeated for all scan lines. Two distinct time axes are evident in this procedure: one representing the time for a single transmission and reception (the depth direction in Fig. 1) and the other representing the time required to receive multiple ensembles for a single scan line (the ensemble direction in Fig. 1). This study refers to these two times as fast time and slow time, respectively.



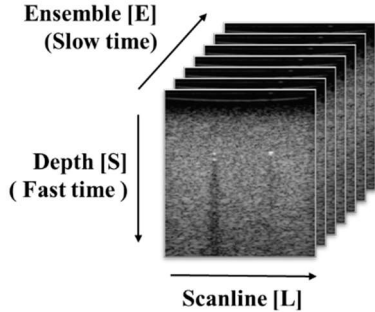


Fig. 1. Illustration of Data receive sequence in color Doppler

Given the limited ensemble length in CDI, efficient clutter filtering and Doppler frequency estimation techniques are crucial. Traditional FIR and IIR filters can be used for clutter filtering when ensemble length is sufficient. However, due to the constraints of ensemble length, techniques such as projected initialized IIR filters have been proposed for CDI [27]. Similarly, for estimating the mean frequency, autocorrelation-based methods are used instead of conventional FFT to address ensemble length limitations [28].

III. Autocorrelation based Doppler classifier

This section introduces a method for automatically classifying TA signals by leveraging their characteristics. The focus lies on distinguishing TA signals from flow signals, which are another major source of Doppler signals observed within the body. To achieve this, the characteristics of TA signals are examined using existing data.



A. Preliminary study

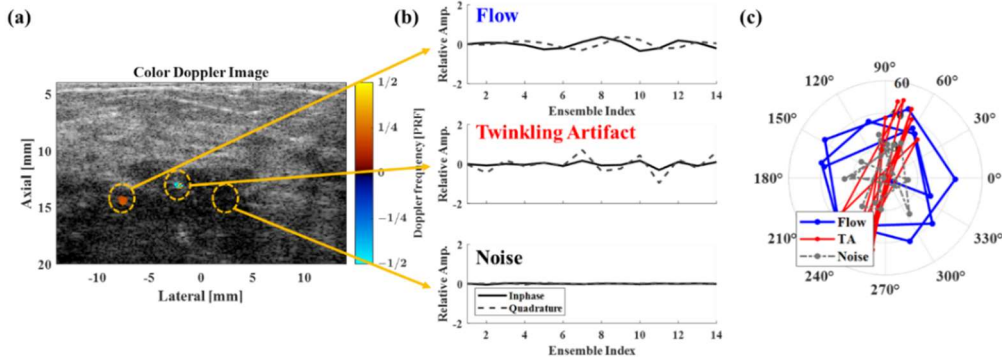


Fig. 2. Signal characteristics of TA, Flow, and Noise. (a) Conventional color Doppler image showing TA, Flow, and Noise. (b) IQ signal plot along the slow-time axis, where the periodic pattern of flow IQ data is absent in both TA and Noise signals. (c) Polar plot of IQ signals, highlighting the randomness of TA and Noise signals.

Fig. 2(a) shows a color Doppler image where targets, presumed to be MCs and blood vessels, are present within the ROI. In this image, three targets highlighted with orange circles are estimated to represent blood flow, MCs, and noise, respectively. Fig. 2(b) presents the slow-time direction signals from the three points marked as orange circle. These signals have been processed by applying a clutter filter to the demodulated IQ signals. In Fig. 2(b), the y-axis indicates the relative intensity of each signal, while the x-axis represents the ensemble index. Solid lines correspond to the in-phase components, and dashed lines represent the quadrature components.

Examining the flow signal in Fig. 2(b), it exhibits a relatively uniform sinusoidal waveform. Additionally, the phase difference between the in-phase and quadrature signals is approximately 90 degrees. From this observation, a hypothesis can be



established that the slow-time spectrum of blood flow signals is characterized by densely distributed sinusoids centered around a specific Doppler frequency.

Conversely, observing the TA component in Fig.2 (b) reveals non-uniform characteristics in both the in-phase and quadrature signals, a feature also observed in noise signals. From this, it can be hypothesized that both TA and noise signals exhibit characteristics like white noise in the frequency spectrum. However, it is also evident that TA signals and noise signals differ in intensity.

The phasor plot of each signal shown in Fig.2(c) reinforces this hypothesis. The flow signal demonstrates the characteristics of a uniformly rotating phasor, whereas TA signals and noise exhibit non-uniform phasor behavior.

B. Autocorrelation based Feature extraction

Based on these observations, it can be hypothesized that flow and TA signals exhibit distinct frequency distributions in the ensemble-direction spectrum. This study proposes an algorithm to distinguish TA signals from flow signals using machine learning, leveraging the differences in their frequency distributions. To this end, the following autocorrelation-based features are extracted.

$$x_1 = \left| Imag \left\{ \frac{R(T)}{R(0)} \right\} \right| \quad (15)$$



$$x_2 = 1 - \text{Real} \left\{ \frac{R(T)}{R(0)} \right\} \quad (16)$$

Where $T = 1/\text{PRF}$, $R(\tau) = \sum_n z(n)z^*(n + \tau)$ and $z(n)$ is the complex signal of the n -th ensemble, and $z^*(n)$ denotes the complex conjugate of $z(n)$

To analyze Equations (15) and (16), the Wiener-Khinchin theorem is applied to express $R(T)$ as the Fourier transform of the power spectral density (PSD) [28]:

$$R(T) = \int_{-\infty}^{\infty} S(f) e^{j2\pi f T} df \quad (17)$$

Here, $j = \sqrt{-1}$. Using the Taylor series expansion, $R(T)$ can be approximated as follows:

$$R(T) = \sum_{n=0}^{\infty} \frac{R^n(0)}{n!} T^n \cong R(0) + T \left\{ \frac{d}{dT} R(T) \Big|_{T=0} \right\} + \frac{T^2}{2} \left\{ \frac{d^2}{dT^2} R(T) \Big|_{T=0} \right\} \quad (18)$$

Substituting Equation (17) into Equation (18), $R(T)$ becomes:

$$R(T) = \int_{-\infty}^{\infty} s(f) df + j2\pi T \int_{-\infty}^{\infty} fs(f) df - 2\pi^2 T^2 \int_{-\infty}^{\infty} f^2 s(f) df \quad (19)$$

Dividing $R(T)$ by $R(0)$ and expanding, we obtain Equation (20). Extracting the real and imaginary components from Equation (20) leads to Equations (21) and (22), respectively:



$$\frac{R(T)}{R(0)} = \frac{\left[\int_{-\infty}^{\infty} s(f) df - 2\pi^2 T^2 \int_{-\infty}^{\infty} f^2 s(f) df \right]}{\int_{-\infty}^{\infty} s(f) df} + \frac{j \left[2\pi T \int_{-\infty}^{\infty} f s(f) df \right]}{\int_{-\infty}^{\infty} s(f) df} \quad (20)$$

$$Imag \left\{ \frac{R(T)}{R(0)} \right\} = \left[2\pi T \frac{\int_{-\infty}^{\infty} f s(f) df}{\int_{-\infty}^{\infty} s(f) df} \right] \quad (21)$$

$$Real \left\{ \frac{R(T)}{R(0)} \right\} = \left[1 - 2\pi^2 T^2 \frac{\int_{-\infty}^{\infty} f^2 s(f) df}{\int_{-\infty}^{\infty} s(f) df} \right] \quad (22)$$

Equations (21) and (22) are related to the mean frequency and the second moment of the PSD, respectively. Applying these equations to the observations in Section 3.1 allows us to infer the distinct characteristics of TA and flow signals. TA signals exhibit random characteristics, which can be modeled as noise uniformly distributed across all frequency bands in the PSD. If the signal density is uniform across all bands, as in TA signals, the PSD is symmetric, resulting in a mean frequency of zero. Furthermore, the wide distribution of the signal leads to a high second moment.

On the other hand, flow signals exhibit higher mean Doppler frequencies corresponding to their velocities, with less spread in the PSD compared to TA signals, resulting in a lower second moment. Based on these inferences, Equations (21) and (22) were reorganized into Equations (15) and (16), forming the hypothesis that these features could differentiate TA and flow signals. This study calculates the proposed features using experimentally obtained TA and flow signals to train a machine learning model.



C. Dataset organization and Classifier training

To validate the derived features, experimental data for TA and flow signals were acquired. As shown in Fig. 3, a phantom mimicking an *in-vivo* environment was fabricated. The phantom included a vessel model simulating blood vessel, an MCs model simulating microcalcifications, and a normal wire as a control target. The entire phantom was completed by pouring a 3% agarose solution to simulate human tissue, as depicted in Fig. 3(a). The placement of the targets within the phantom is shown in Fig. 3(b). Fig. 3(c), 3(d), and 3(e) respectively display the B-mode, Power Doppler, and Color Doppler images of the fabricated phantom. The MCs model displayed an irregular color Doppler pattern due to TA signals, while the rightmost target showed no significant Doppler signals apart from residual clutter. These observations confirm that the constructed phantom provides all necessary signals for testing the proposed algorithm.



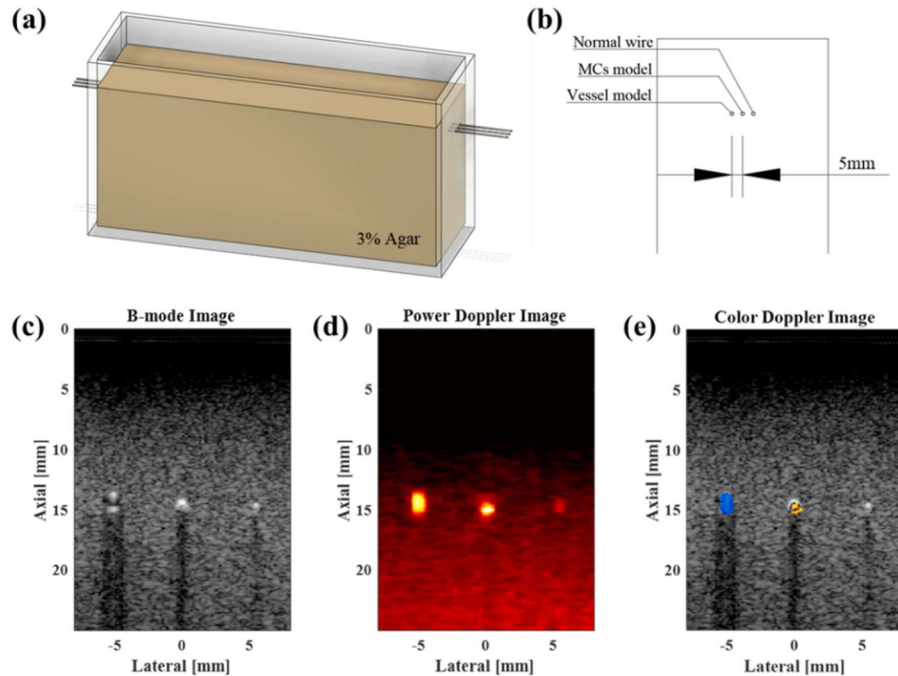


Fig. 3. Phantom setup for machine learning dataset. (a) The phantom consists of three targets and is filled with 3% agarose. (b) The vessel model, MCs model, and a normal wire are arranged within the phantom as shown. (c) B-mode imaging of the phantom clearly visualizes the three targets. (d) Power Doppler imaging detects Doppler signals from the flow and MCs models. (e) In the color Doppler image, an irregular color pattern is observed in the MCs model, while a smooth color pattern is seen in the flow model.

The TA and flow signals were acquired under varying PRF and flow velocity conditions to prevent overfitting to specific parameters. This ensured the robustness of the algorithm across different transmission and reception environments. The parameters used in this experiment are summarized in Table 1. Detailed descriptions of the experimental setup are provided in the later.



Table 1
Experimental parameters for dataset organization

Parameter	PRF sweep	Flow speed sweep
PRF	$\{5, 6, 7, 8, 9\}$ kHz	4kHz
Flow velocity	40ml/min	$\{20, 25, 30, 35, 40\}$ ml/min
Ensembles length		16
# of Cycle		6
Tx Freq.		5MHz
TX Voltage		30.3V (60 Vpp)
Total number of frames		300
Data point for each frame		15

For the acquired data, TA and flow regions were identified, and data from the central regions of each were extracted and labeled. The proposed features were then calculated for the labeled data. Since the features are derived from the entire ensemble data, each feature value was derived from 16 complex samples.

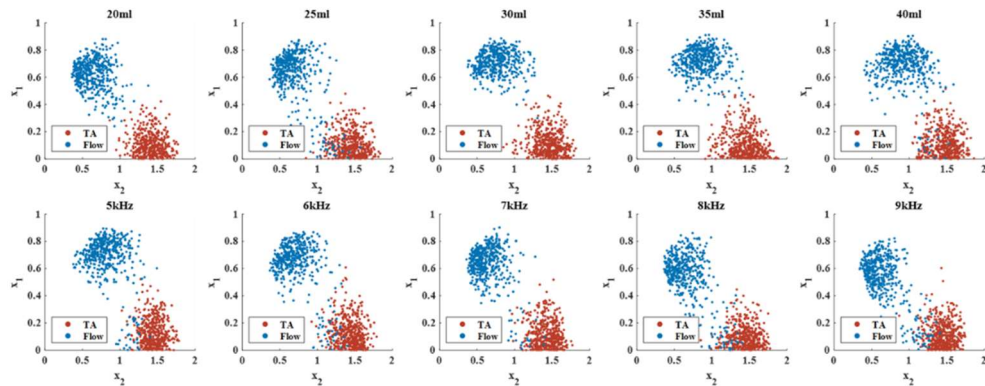


Fig. 4. Scatter plot of extracted features from the dataset for each parameter. The x-axis represents the second moment of ensemble data, with higher values observed for TA compared to Flow. The y-axis represents the average Doppler frequency, with lower values observed for TA compared to Flow.

Fig. 4 illustrates the scatter plot of the dataset after labeling and feature extraction. This plot indicates that the proposed features effectively separate the signals under various parameters. Analyzing the scatter plot in detail, the vertical axis corresponds to the mean frequency (x_1) derived from Equation (15). TA signals predominantly showed values near zero, while flow signals exhibited relatively higher values. The horizontal axis corresponds to the second moment (x_2) from Equation (16). TA signals displayed higher second moments, while flow signals showed comparatively lower values. These experimental results align with the hypotheses proposed in Section 3.2. Although some overlap was observed, where flow signals appeared in TA regions, these instances were not dominant and were generally limited, and the signals were well-separated in most instances. Thus, the extracted features were deemed suitable, forming the basis for training the machine learning algorithm.

Table 2 presents the results of training four machine learning models using the extracted features. All models achieved an accuracy above 95%, with support vector machines (SVM) and quadratic discriminant models achieving accuracies exceeding 97%.

Table 2
Validation accuracy of the dataset for each model

Model	Accuracy [%]
KNN	95.6
SVM	97.2
Quadratic Discriminant	97.0
Naïve bayes	97.1



IV. Multi band Doppler imaging

The Doppler classifier proposed in Chapter 3 effectively distinguishes between flow and TA signals. However, it has limitations in separating TA from noise signals, as the proposed features yield similar values for both. Specifically, both noise and TA signals exhibit nearly zero mean PSD frequencies and high second moments. To differentiate TA signals from noise, their high signal intensity characteristics must be utilized. However, in environments with limited SNR or insufficiently strong TA signals, visualizing TA distinctively can be challenging. Therefore, even after flow is classified, it is essential to suppress noise and enhance TA signals to ensure high sensitivity in TA detection. This chapter introduces a Multi-Band Doppler Imaging (MBDI) technique to address this issue, including the hypothesis and signal processing methods underpinning this approach [29].

A. Hypothesis

As noted, improving the sensitivity of TA detection requires enhancing the SNR of TA signals. This study focuses on the nonlinear characteristics of TA signals, which generate specific Doppler signals even without object movement [17-18]. Such nonlinear characteristics are hypothesized to influence the spectral characteristics of the signal in the fast-time direction, potentially broadening the spectrum. Based on this, the study hypothesizes that TA signals exhibit spectral broadening in the fast-time direction, approximating the probe's reception bandwidth. Leveraging these characteristics, the



study proposes a method to suppress noise and adaptively enhance TA signals through their spectral features.

B. MBDI signal block

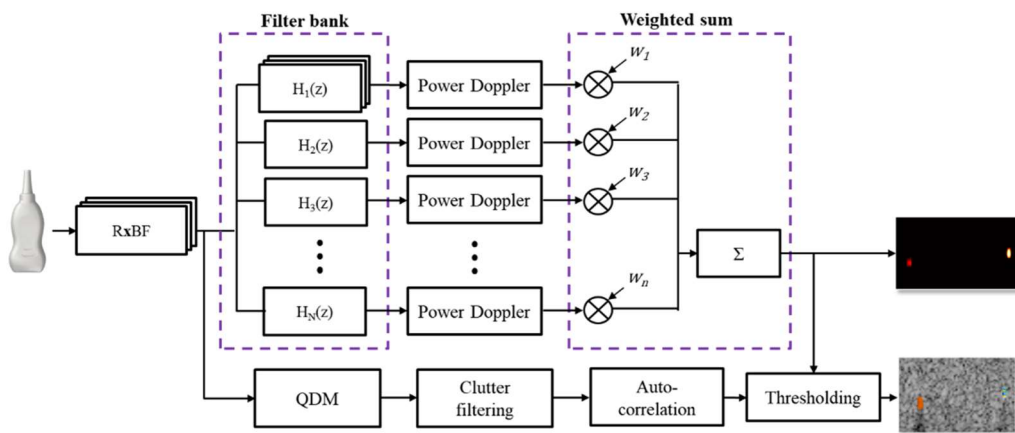


Fig. 5. Overall signal processing block diagram. The Multi-Band Doppler Imaging (MBDI) method comprises a filter bank and weighted sum. The filter bank decomposes the radio frequency (RF) signal into multiple spectral bands. The weighted summation enhances the TA signal while reducing noise signals.

Fig. 5 illustrates the overall signal flow of the proposed MBDI technique. The process comprises two primary components: a filter bank for signal decomposition and a weighted sum module for recombining the decomposed signals. Signal decomposition involves separating the received focused signal into frequency bands in the fast-time direction, enabling the utilization of TA signal features across bands. After decomposition, power Doppler imaging is applied to each band, followed by weighting based on predefined weights. Bands with higher TA signal intensity receive larger

weights, while those dominated by noise receive smaller weights. This approach produces an adaptively enhanced power Doppler image of TA signals.

C. Filter bank

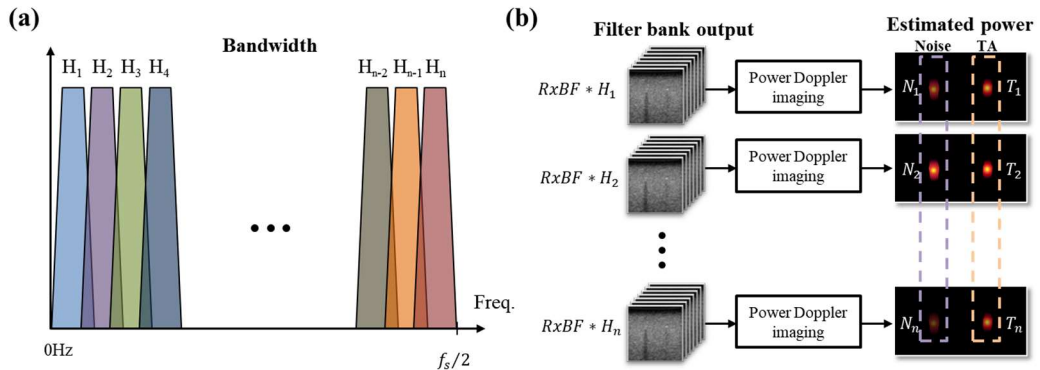


Fig. 6. Illustration of filter bank structure and output data. (a) the filter bank comprises n FIR filters with equal passband width (b) Power doppler imaging is applied to the filtered data. Due to the distinct spectral characteristics of Noise and TA, the estimated power patterns differ across multiple frequency bands.

The first step of the MBDI technique is to decompose the received signal using n -bandpass filters. As shown in Fig. 6(a), the filters have n evenly divided passbands and are applied in the fast-time direction to separate spectral components. After decomposition, each band undergoes power Doppler imaging, as depicted in Fig. 6(b), yielding the Doppler signal intensity for each frequency band. The TA signal power Doppler intensities are denoted as \bar{T} , and the noise intensities as \bar{N} , defined by Equations (23) and (24).

$$\bar{T} = [T_1 \ T_2 \ T_3 \ \dots \ T_n]^T \quad (23)$$

$$\bar{N} = [N_1 \ N_2 \ N_3 \ \dots \ N_n]^T \quad (24)$$

D. Signal modeling and weight optimization

After decomposition and power Doppler computation, the signals are recombined using optimal weights.

$$\underset{\bar{w}}{\text{maximize}} \quad (\bar{T} - \bar{N})^T \cdot \bar{w} \quad (25)$$

The weights must satisfy Equation (25), which aims to maximize the dot product of \bar{T} and the weights while minimizing the dot product of \bar{N} and the weights. However, since \bar{T} and \bar{N} are unknown for unseen data, this study proposes a model-based approach for these vectors.



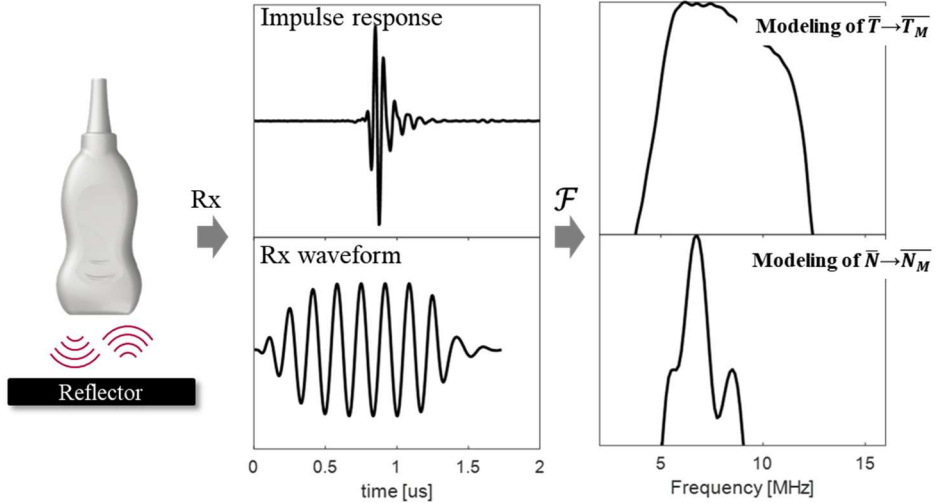


Fig. 7. Concept of signal vector modeling method. The array vector \bar{T} is modeled based on the probe's impulse response, under the hypothesis that the spectrum of TA closely resembles the probe's impulse response. Additionally, the vector \bar{N} is modeled using the received signal spectrum of the transmit pulse.

Fig. 7 illustrates the modeling concept. The TA spectral response is modeled using the probe's frequency response, while the noise is modeled as the ideal received waveform spectrum of the transmitted signal. This modeling approach accounts for residual clutter signals in noise and minimizes white noise in the optimization process.

$$\begin{aligned} & \underset{\bar{w}}{\text{maximize}} \quad (\bar{T}_M - \bar{N}_M)^T \cdot \bar{w} \\ & \text{subject to} \quad \|\bar{w}\| \leq 1 \end{aligned} \quad (26)$$

Substituting the modeled vectors into Equation (25) yields Equation (26), which introduces constraints to prevent weight divergence and suppress weights outside the TA spectrum, minimizing white noise.

E. Visualization

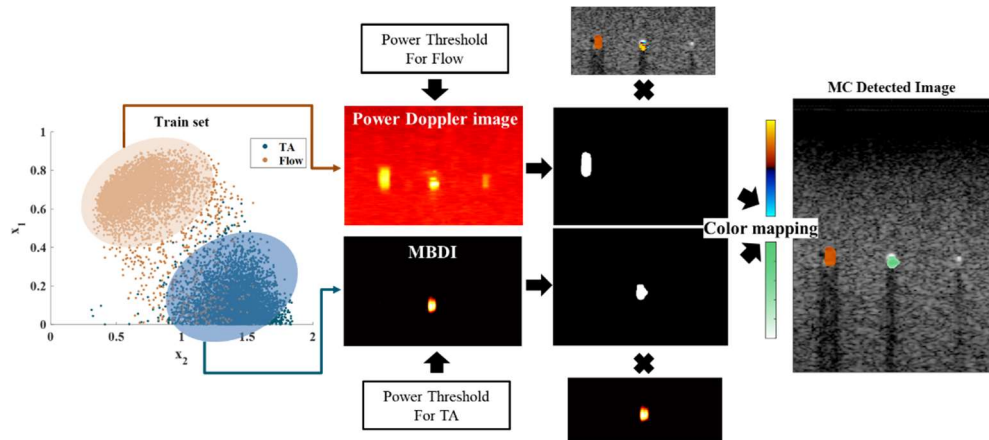


Fig. 8. Visualization of the Proposed Method. Flow signals are initially classified and thresholded, followed by region mapping using conventional color Doppler techniques. The MBDI method is applied to regions classified as TA. This process produces a TA-enhanced power Doppler map, which can be visualized using a distinct color map.

Fig. 8 demonstrates the visualization method using the proposed technique. First, features are extracted as described in Chapter 3. Flow signals are classified and thresholded to generate a standard color Doppler image using autocorrelation. For regions identified as TA, signals are enhanced using MBDI, thresholded, and mapped to corresponding power values and colors. The final visualization overlays these results onto B-mode images, assigning green to TA regions for clear differentiation from the color Doppler signals.

This visualization technique enhances MC signals and integrates them into color Doppler imaging. It not only aids in detecting MCs in early-stage breast cancer but also



enhances diagnostic value by visualizing vessels, such as those involved in angiogenesis, alongside these signals.

V. Experimental result

A. Experimental setup

To validate the proposed method, this study conducted both *in-vitro* and *in-vivo* experiments. This section describes the experimental setups.

In-vitro experiment

Fig. 9 illustrates the fabrication of the phantom used in the experiments. Fig. 9(a) shows calcium oxalate adhered to a wire to simulate MCs, serving as the target generating TA signals [21]. Fig. 9(b) depicts the MCs model and vessel model placed together within an acrylic mold. After confirming that both targets were included within the ROI, as shown in Fig. 9(c), a 3% agar solution was poured to mimic an in vivo environment. Using commercial equipment to image the phantom, Fig. 9(d) confirms that Doppler signals from blood flow and TA signals from MCs are both clearly visible.



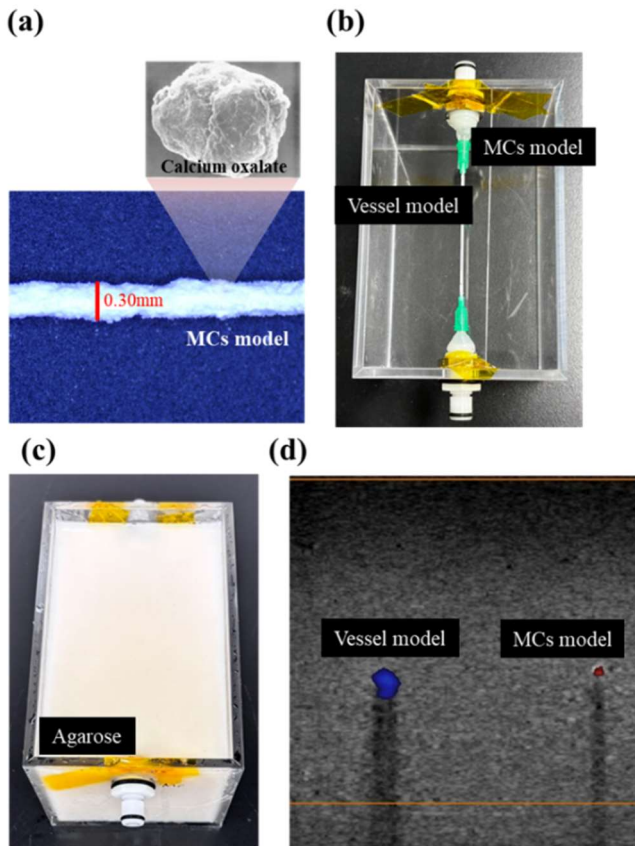


Fig. 9 Fabrication of the Phantom. (a) To simulate MCs, a wire was coated with calcium oxalate to create the MC model. (b) The fabricated MC model was placed in the phantom along with a vessel model for blood flow simulation. (c) The phantom was completed by filling it with 3% agarose. (d) Using a commercial ultrasound system, imaging of the completed phantom successfully captured Doppler signals for both TA and Flow.

Fig. 10 shows the process of applying blood flow to the phantom and acquiring data. Blood flow was simulated using a blood-mimicking fluid (Shelly Medical, London, Ontario, Canada) pumped through the system using a syringe pump (kdScientific, Holliston, MA, USA). Data was received using a Vantage 128 system (Verasonics,

Kirkland, WA, USA) and processed on a computer with MATLAB. Detailed transmission and reception parameters are provided in Table 3.

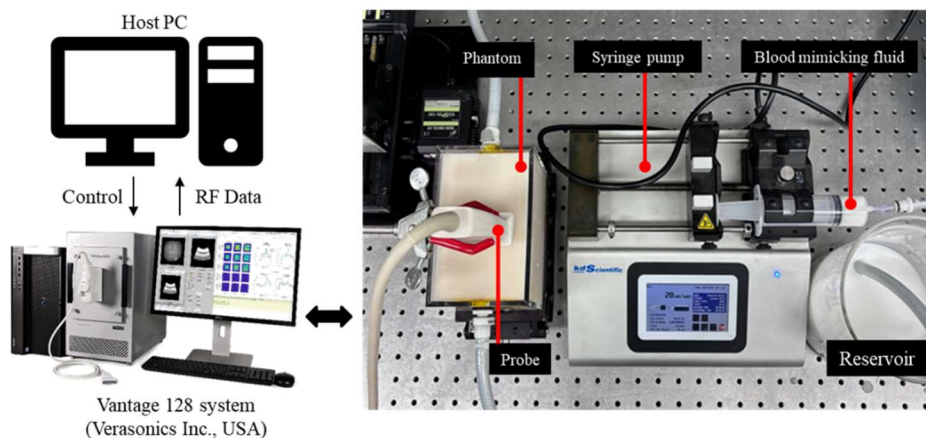


Fig. 10 Experimental setup using the fabricated phantom. The experiment was conducted by transmitting and receiving data using a research-grade ultrasound platform.

Table 3.
Transmit-Receive parameters for experiment

Parameters	Value
Probe	L11-5v
TX frequency [MHz]	6.3
Tx F number	1.2
Rx F number	1.5
# of ensemble	14
PRF	3 kHz

The MBDI method was quantitatively evaluated using an SNR-based metric, defined in Equation (27):

$$SNR = 20 \log_{10} \left(\frac{\mu_{TA}}{\mu_{Noise}} \right) \quad (27)$$

Here, μ_{TA} and μ_{Noise} represent the average signal intensities in the TA and noise regions, respectively.

In-vivo experiment

Based on the *in-vitro* results, an *in-vivo* experiment was conducted at Yonsei University's Severance Hospital. Ultrasound transmission and reception were performed using RS80 and Z20 systems (Samsung Medison, Seoul, Republic of Korea), with subsequent processing in MATLAB. Since these commercial systems could not capture radio frequency (RF) signals, the MBDI method was not applied. Instead, results were generated using the autocorrelation-based Doppler classifier.

B. Experimental results

In-vitro result



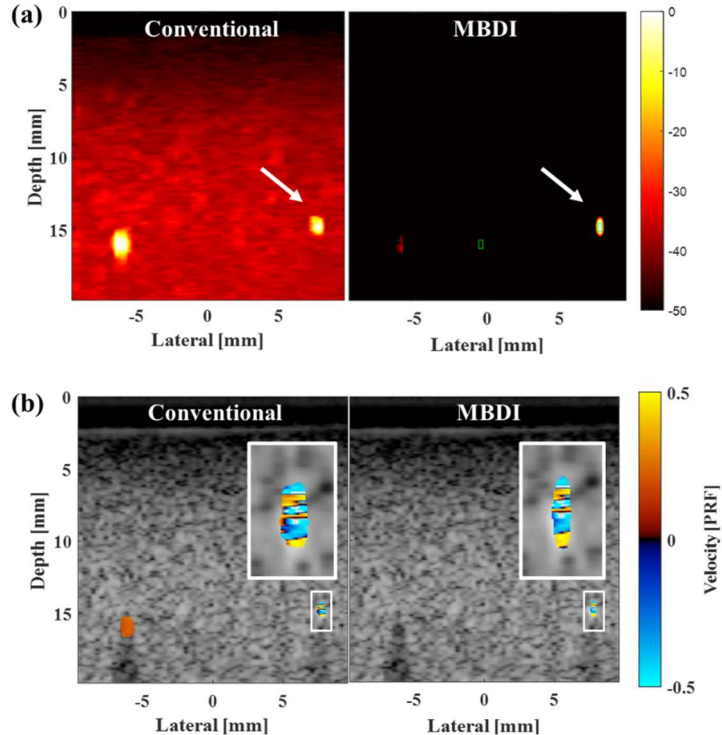


Fig. 11. Qualitative results of the MBDI method. (a) Power Doppler results with the MBDI method show enhanced signals in the TA region, highlighted by white arrows, compared to surrounding noise signals. (b) Color Doppler results with the MBDI method demonstrate that the irregular Doppler pattern in the TA region is preserved and amplified.

Fig. 11 compares the proposed MBDI method with existing techniques after Doppler ultrasound was applied to the phantom. Fig. 11(a) shows a power Doppler image enhanced by the MBDI method, with MCs visualized in the areas marked by white arrows. The results demonstrate that TA Doppler signals from MCs are amplified with the proposed MBDI method. A decrease in signal intensity of the flow region was

observed, attributed to the enhancement of TA signals. However, this does not affect visualization, as flow is separately classified before visualization.

Table 4.
quantitative result of MBDI method

Methods	SNR
Conventional	34.38 ± 0.89
MBDI	144.51 ± 3.12

Table 4 summarizes SNR measurements taken from the green-labeled TA regions and noise regions, averaging over five measurements. The SNR of the proposed method shows an increase of over 110 dB compared to existing techniques. Fig. 11(b) displays the thresholded color Doppler image derived from the enhanced power map, preserving TA's characteristic irregular color patterns.



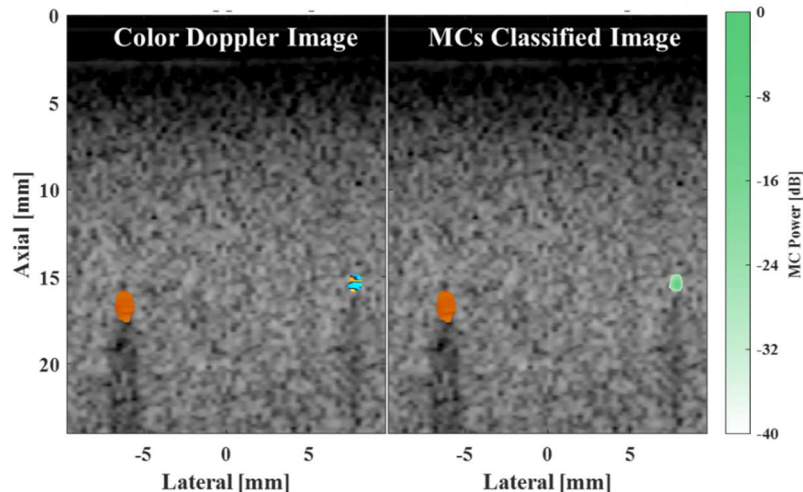


Fig. 12. Result image of proposed Doppler classifier. The TA signal, simulated using the MC model, was automatically classified and emphasized as a TA signal, while the blood flow signal was comprehensively represented with it.

Fig. 12 demonstrates the application of the proposed Doppler classifier to the enhanced signals. TA signals generated by the MCs model are distinctly visualized in green, clearly differentiating them from other signals.

In-vivo result

This study also conducted *in-vivo* experiments. However, due to the limitations of commercial ultrasound equipment, which cannot extract RF signals, the results from these experiments include only the Doppler classifier's performance.



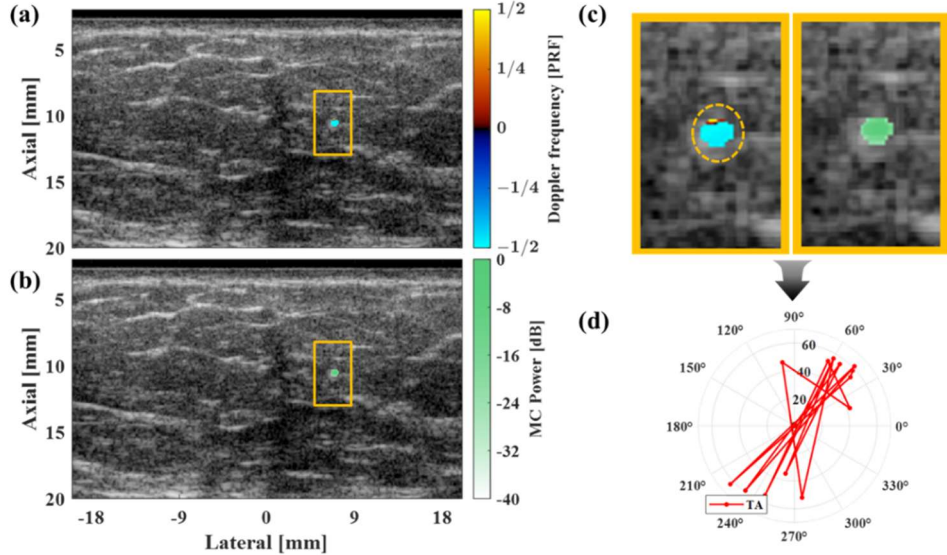


Fig. 13. Experimental results of *in-vivo* breast. (a) Conventional color Doppler image. (b) TA signal classified using the proposed Doppler classifier. (c) Scaled view of the orange-boxed region. (d) Polar plot of the orange-dotted circular region. The area showing TA characteristics in the polar plot was also classified as TA by the proposed classifier.

Fig. 13 illustrates the results of applying the Doppler classifier to *in-vivo* data. Fig. 13(a) and Fig. 13(b) display the conventional color Doppler image and the results after applying the Doppler classifier, respectively. Zoomed views of the orange box in these images are presented in Fig. 13(c). Additionally, a phasor plot for the region suspected to be MCs is shown in Fig. 13(d). As depicted in Fig. 13(a), The irregular color Doppler pattern is presented in a small part of the target in the color Doppler image, while the phasor plot exhibits the characteristics of a TA signal. However, the classifier accurately categorized this region as TA, as indicated by the green mapping.

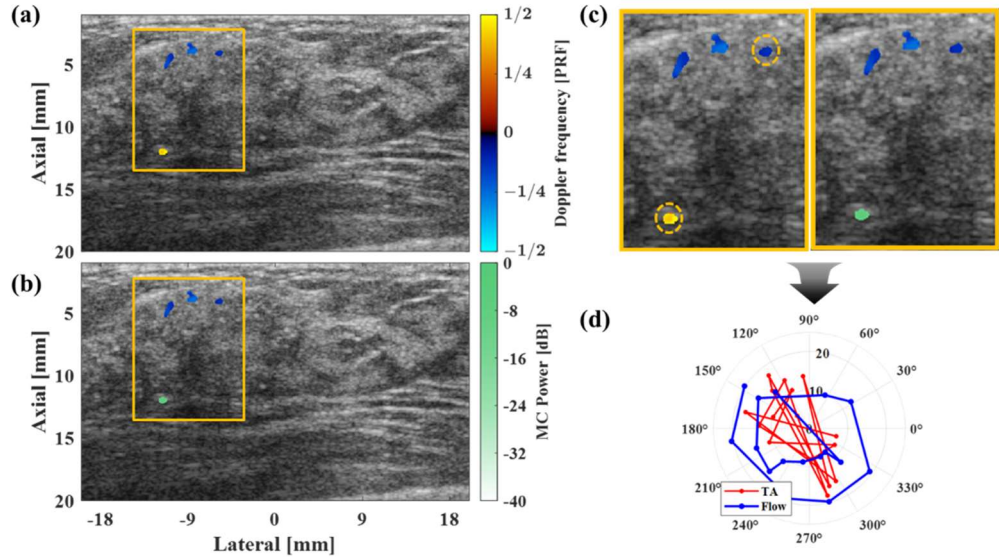


Fig. 14. Experimental results from *in-vivo* study. (a) Conventional color Doppler image. (b) TA signal classified using the proposed Doppler classifier. (c) Scaled view of the orange-boxed region. (d) Polar plot of the orange-dotted circular region. The region exhibiting TA characteristics in the polar plot was classified as TA, while the region showing flow characteristics was classified as flow.

Fig. 14 presents similar results, showing the color Doppler image, classifier results, and phasor plots for various targets. The upper and lower regions in Fig. 14(c) exhibit similar Doppler patterns in the color Doppler image. However, the classifier identified the lower target as a TA signal, represented in green. In contrast, the three upper targets were classified as flow signals. Phasor plots of these regions show random distributions for the TA-classified signals, consistent with TA characteristics, while the flow-classified targets exhibited relatively uniform phasor rotations.

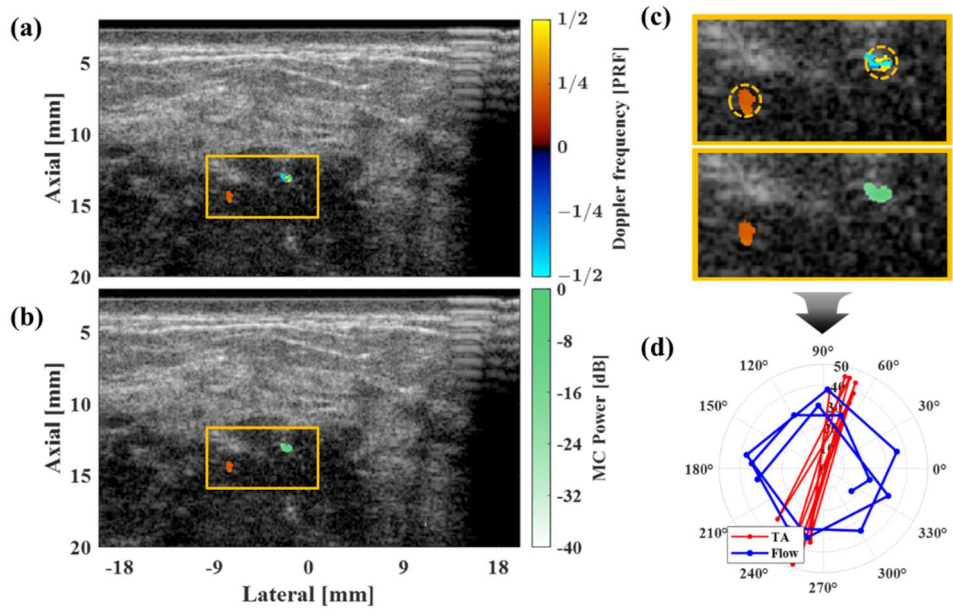


Fig. 15. Experimental results from *in-vivo* study. (a) Conventional color Doppler image. (b) TA signal classified using the proposed Doppler classifier. (c) Scaled view of the orange-boxed region. (d) Polar plot of the orange-dotted circular region. The region exhibiting TA characteristics in the polar plot was classified as TA, while the region showing flow characteristics was classified as flow.

Fig. 15 depicts another case. In this instance, the suspected TA signal in the right ROI displayed characteristic uneven patterns in the color Doppler image. The classifier confirmed this signal as TA. Meanwhile, phasor plots of the left (flow) and right (TA) targets reveal that the flow signal exhibited nearly circular phasor rotation, whereas the TA signal did not.

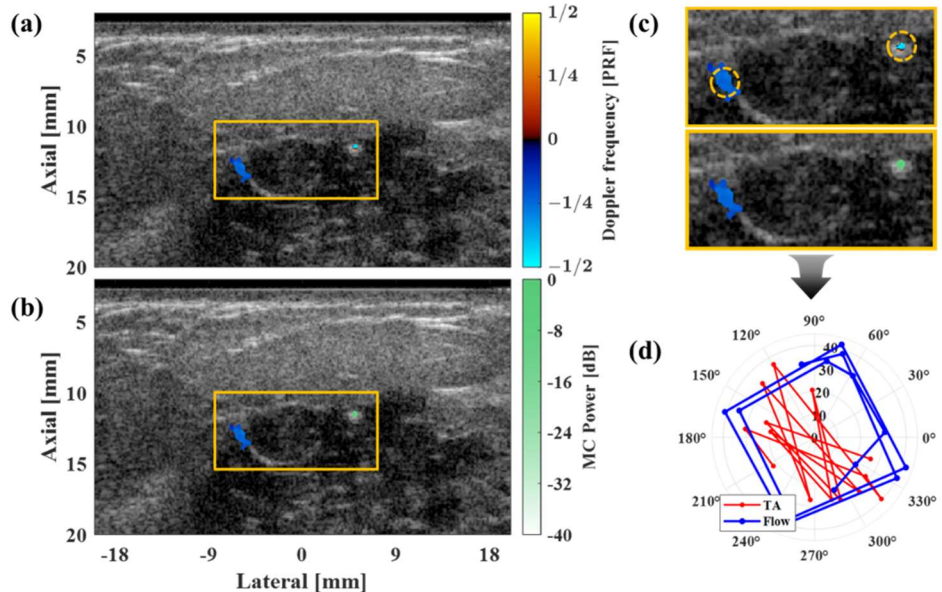


Fig. 16. Experimental results from *in-vivo* study. (a) Conventional color Doppler image. (b) TA signal classified using the proposed Doppler classifier. (c) Scaled view of the orange-boxed region. (d) Polar plot of the orange-dotted circular region. The region exhibiting TA characteristics in the polar plot was classified as TA, while the region showing flow characteristics was classified as flow.

Fig. 16 shows another case. Among the two targets in the ROI, the right target was identified as TA, and the left as flow. Phasor plots confirm the classification, with the flow signal showing circular rotation and the TA signal displaying irregular phasor progression.

VI. Discussion and Conclusions

A. Discussion

Contributions

This paper discusses a safe and efficient approach for detecting MCs in the breast using ultrasound imaging devices. Specifically, it introduces an algorithm for MCs detection leveraging TA. The proposed method enhances signals primarily induced by MCs and automates their detection via an algorithm. This study contributes significantly by proposing machine-learning-based Doppler signal classifier and signal enhancement using MBDI.

The Doppler signal classifier extracts features based on the relationship with autocorrelation. Experimental results demonstrate a high accuracy of 97% on the training dataset. Furthermore, inference on unseen *in-vivo* datasets yielded results consistent with phasor-observed signal characteristics. Notably, this algorithm achieves computational efficiency by directly utilizing intermediate results from autocorrelation, a common process in color Doppler imaging. Quantitative signal classification methods like this not only offer potential diagnostic criteria but also show promise for integration into automated screening systems like Automated Breast Ultrasound System (ABUS).

The MBDI technique leverages spectral broadening along the fast-time direction to enable adaptive enhancement of TA signals across frequency bands. Experimental findings revealed a significant Signal-to-Noise Ratio (SNR) improvement of



approximately 110 dB. This enhancement was also validated in both power Doppler and color Doppler images, suggesting its compatibility with the classifier for high-performance applications.

Limitations

Several limitations of the proposed methods are identified in this study. First, there is a lack of comprehensive understanding of the physical mechanisms underlying TA generation. Although previous studies have explored this phenomenon [30-33], definitive explanations remain elusive. A more robust understanding of TA origins could facilitate the utilization of a wider range of TA characteristics. Specifically, elucidating the reasons behind TA spectral broadening may lead to broader applicability.

Second, the *in-vivo* experimental results are insufficient. As mentioned earlier, limitations in the ultrasound equipment used in this study hindered a comprehensive evaluation of the MBDI technique. Similarly, the classifier's performance on *in-vivo* data was constrained by the limited dataset size. Comparing *in-vivo* results with biopsy-derived ground truth is expected to yield valuable insights for future studies.



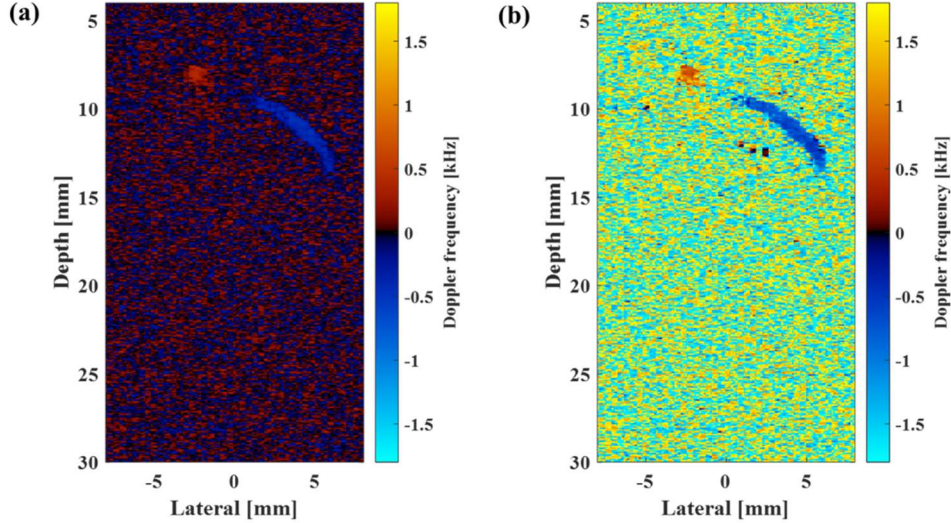


Fig. 17 Comparison of the proposed method and conventional average frequency estimation methods. (a) Visualization of the x_1 feature, representing the average frequency extracted as one of the proposed classifier's features, mapped onto the image. (b) Visualization of the Doppler frequency mapped onto the image using traditional average frequency estimation methods. These images were derived from *in-vivo* experimental data, specifically frames capturing breast vasculature. In both images, regions corresponding to blood flow exhibit similar values, whereas areas presumed to represent background noise show significantly different values.

Further investigation is necessary to understand the proposed classifier's method for average frequency estimation. This study suggested that the imaginary component of the ratio of Lag-1 autocorrelation to Lag-0 autocorrelation represents the average frequency. It was demonstrated that the estimated average frequency exhibits small values for noise and TA signals, making it a useful metric for distinguishing blood flow signals. However, when estimating the average frequency of noise using conventional methods [28], the values are relatively large, approximating PRF/2. This phenomenon is



illustrated in Fig. 17. Fig. 17 visualizes a frame from in-vivo data capturing breast vasculature using both methods. Fig. 17(a) depicts the average Doppler frequency visualized through the proposed method, where noise regions exhibit values close to zero, consistent with the study's assumptions. In contrast, Fig. 17(b) represents the average Doppler frequency estimated using a conventional method, where noise regions show high values and blood flow regions reflect flow velocity. This intriguing phenomenon suggests that, while both methods use autocorrelation to estimate the mean value of the Doppler frequency PSD, they yield different results when the signal exhibits random characteristics. This is presumed to result from the use of different approximation techniques employed by the two methods. Further research is required to elucidate the underlying cause of this discrepancy.

B. Conclusions

This research highlights the limitations of mammography, a prevalent screening method for early breast cancer detection, and proposes an alternative using ultrasound imaging devices. It introduces methods for TA signal enhancement and classification to provide comprehensive diagnostic information. The proposed techniques demonstrated high performance in *in-vitro* experiments and showed partial feasibility in *in-vivo* applications.

Through further validation in subsequent studies, these methods could move closer to clinical implementation. Notably, this study focuses on detecting TA within human



tissues and improving the sensitivity of MC detection, distinguishing it from previous research. With sufficient investigation, the proposed approach holds promise for practical use in clinical settings.



Reference

1. Harbeck, N., et al., *Breast cancer*. Nat Rev Dis Primers, 2019. **5**(1): p. 66.
2. Cao, W., et al., *Comparative study of cancer profiles between 2020 and 2022 using global cancer statistics (GLOBOCAN)*. J Natl Cancer Cent, 2024. **4**(2): p. 128-134.
3. Xu, Y., et al., *Global trends and forecasts of breast cancer incidence and deaths*. Sci Data, 2023. **10**(1): p. 334.
4. ADAIR, F.E., *Clinical manifestations of early cancer of the breast*. New England Journal of Medicine, 1933. **208**(24): p. 1250-1255.
5. Giaquinto, A.N., et al., *Breast Cancer Statistics, 2022*. CA Cancer J Clin, 2022. **72**(6): p. 524-541.
6. Elmore, J.G., et al., *Screening for breast cancer*. Jama, 2005. **293**(10): p. 1245-1256.
7. Waks, A.G. and E.P. Winer, *Breast Cancer Treatment: A Review*. JAMA, 2019. **321**(3): p. 288-300.
8. Balleyguier, C., et al., *BIRADS classification in mammography*. Eur J Radiol, 2007. **61**(2): p. 192-4.



9. Castellaro, A.M., et al., *Oxalate induces breast cancer*. BMC Cancer, 2015. **15**: p. 761.
10. Gal, S., M.J. Pavan, and N. Vidavsky, *Characterization of dolomite and calcite microcalcifications in human breast tissue*. RSC Adv, 2024. **14**(39): p. 28741-28752.
11. Nahmias, Y., G. Yazbek Grobman, and N. Vidavsky, *Inhibiting Pathological Calcium Phosphate Mineralization: Implications for Disease Progression*. ACS Appl Mater Interfaces, 2024. **16**(15): p. 18344-18359.
12. Beemsterboer, P.M., et al., *Radiation risk of mammography related to benefit in screening programmes: a favourable balance?* Journal of medical screening, 1998. **5**(2): p. 81-87.
13. Kerlikowske, K., et al., *Effect of age, breast density, and family history on the sensitivity of first screening mammography*. Jama, 1996. **276**(1): p. 33-38.
14. Aro, A.R., et al., *Pain and discomfort during mammography*. European Journal of Cancer, 1996. **32**(10): p. 1674-1679.
15. Jensen, J.A., *Medical ultrasound imaging*. Prog Biophys Mol Biol, 2007. **93**(1-3): p. 153-65.



16. Geisel, J., M. Raghu, and R. Hooley, *The Role of Ultrasound in Breast Cancer Screening: The Case for and Against Ultrasound*. Semin Ultrasound CT MR, 2018. **39**(1): p. 25-34.
17. Rahmouni, A., et al., *Color Doppler twinkling artifact in hyperechoic regions*. Radiology, 1996. **199**(1): p. 269-271.
18. Wang, M., et al., *Systematic analysis of factors related to display of the twinkling artifact by a phantom: an optimized investigation*. Journal of Ultrasound in Medicine, 2011. **30**(11): p. 1449-1457.
19. Chelfouh, N., et al., *Characterization of urinary calculi: in vitro study of "twinkling artifact" revealed by color-flow sonography*. AJR. American journal of roentgenology, 1998. **171**(4): p. 1055-1060.
20. Leonov, D.V., et al., *Detection of Microcalcifications using the Ultrasound Doppler Twinkling Artifact*. Biomedical Engineering, 2020. **54**(3): p. 174-178.
21. Kang, J., et al., *3D microcalcification detection using a color Doppler twinkling artifact with optimized transmit conditions: Preliminary results*. Med Phys, 2020. **47**(12): p. 6171-6178.
22. Kang, J., et al., *Real-Time Ultrasound Detection of Breast Microcalcifications Using Multifocus Twinkling Artifact Imaging*. IEEE Trans Med Imaging, 2022. **41**(5): p. 1300-1308.



23. Powers, J. and F. Kremkau, *Medical ultrasound systems*. Interface Focus, 2011. **1**(4): p. 477-89.
24. Evans, D.H., J.A. Jensen, and M.B. Nielsen, *Ultrasonic colour Doppler imaging*. Interface focus, 2011. **1**(4): p. 490-502.
25. Newhouse, V.L., P.J. Bendick, and W. Varner, *Analysis of transit time effects on Doppler flow measurement*. IEEE Transactions on Biomedical Engineering, 1976(5): p. 381-387.
26. Brody, W.R. and J.D. Meindl, *Theoretical analysis of the CW Doppler ultrasonic flowmeter*. IEEE transactions on biomedical engineering, 1974(3): p. 183-192.
27. Yoo, Y.M., R. Managuli, and Y. Kim, *Adaptive clutter filtering for ultrasound color flow imaging*. Ultrasound Med Biol, 2003. **29**(9): p. 1311-20.
28. Kasai, C., et al., *Real-time two-dimensional blood flow imaging using an autocorrelation technique*. IEEE Transactions on sonics and ultrasonics, 1985. **32**(3): p. 458-464.
29. Seongjun Park, Y.Y. *A Multi Band Doppler Imaging Based Microcalcification Detection Method for Early Breast Cancer Identification* in *KOSOMBE*. 2024. Seoul.



30. Lu, W., et al., *Evidence for trapped surface bubbles as the cause for the twinkling artifact in ultrasound imaging*. Ultrasound in medicine & biology, 2013. **39**(6): p. 1026-1038.
31. Aytaç, S.K., and Hasan Özcan, *Effect of color Doppler system on the twinkling sign associated with urinary tract calculi*. Journal of Clinical Ultrasound, 1999. **27**(8): p. 433-439.
32. Leonov, D.V., et al., *Causes of Ultrasound Doppler Twinkling Artifact*. Acoustical Physics, 2018. **64**(1): p. 105-114.
33. Simon, J.C., et al., *The role of trapped bubbles in kidney stone detection with the color Doppler ultrasound twinkling artifact*. Phys Med Biol, 2018. **63**(2): p. 025011.

